

An Integrated Photonic Platform for Rare-Earth Ions in Thin Film Lithium Niobate

Subhojit Dutta¹, Elizabeth A. Goldschmidt², Sabyasachi Barik¹, Uday Saha¹, Edo Waks^{1*}

¹*Department of Electrical and Computer Engineering, Institute for Research in Electronics and Applied Physics, and Joint Quantum Institute, University of Maryland, College Park, MD 20742, USA.*

²*Department of Physics, University of Illinois at Urbana-Champaign, Urbana, IL 61801*
**edowaks@umd.edu*

Abstract. Rare-earth ion ensembles doped in single crystals are a promising materials system with widespread applications in optical signal processing, lasing, and quantum information processing. Incorporating rare-earth ions into integrated photonic devices could enable compact lasers and modulators, as well as on-chip optical quantum memories for classical and quantum optical applications. To this end, a thin film single crystalline wafer structure that is compatible with planar fabrication of integrated photonic devices would be highly desirable. However, incorporating rare-earth ions into a thin film form-factor while preserving their optical properties has proven challenging. We demonstrate an integrated photonic platform for rare-earth ions doped in a single crystalline thin film on insulator. The thin film is composed of lithium niobate doped with Tm^{3+} . The ions in the thin film exhibit optical lifetimes identical to those measured in bulk crystals. We show narrow spectral holes in a thin film waveguide that require up to 2 orders of magnitude lower power to generate than previously reported bulk waveguides. Our results pave way for scalable on-chip lasers, optical signal processing devices, and integrated optical quantum memories.

Keywords: rare-earth ions, thin film lithium niobate, integrated photonics, spectral hole burning, quantum information processing, optical signal processing

Rare-earth ion dopants are solid-state emitters that have found widespread uses in both classical and quantum optics¹⁻⁴. These emitters exhibit stable optical transitions with long lifetimes, making them a useful gain material for lasers and optical amplifiers^{4,5}. They also feature narrow homogeneous linewidths,^{6,7} which find broad applications in optical signal processing as high finesse filters for laser phase noise suppression,^{4,8} and medical imaging⁹. Due to their long coherence times¹⁰, rare-earth ions are also promising candidates for optical quantum memories¹¹ and qubits¹², which are essential components of quantum networks¹³ and distributed quantum computers¹⁴.

The incorporation of rare-earth ions into integrated photonics could enable a new class of active opto-electronic systems with applications in classical and quantum information processing. Integrated photonics combines many optical components on a compact chip, which is essential for scalability and device efficiency. However, incorporating rare-earth ions into integrated photonic devices has proved challenging because these emitters typically reside in bulk crystals^{1,4,8}, which are not compatible with conventional planar fabrication techniques¹⁵. One effective solution is to directly pattern integrated photonic devices into the bulk either by ion milling¹⁶⁻¹⁸ or by ion diffusion to form waveguides^{1,19}. Hybrid integration²⁰⁻²², where nanostructures are evanescently coupled to rare-earth ions in the bulk, provides another promising approach. Implanting rare-earth ions into materials that are compatible with planar fabrication, such as Er³⁺ implanted in silicon nitride^{23,24}, has been demonstrated, but the homogeneous linewidth is broadened even at cryogenic temperatures^{24,25}. A thin film material platform that is single crystalline and preserves the bulk properties of the emitter is therefore critically lacking.

Lithium niobate provides a promising host material for rare-earth ion integrated photonics¹. Rare-earth doped channel waveguides in lithium niobate have been used to realize lasers^{26,27} and quantum memories^{19,28,29} spanning a vast range of wavelengths from the infrared to the telecom band. Furthermore, lithium niobate is compatible with commercial wafer scale smart-cut which enables thin single crystalline films on oxide, a lower index material that can support low loss waveguides³⁰ and also act as a sacrificial layer^{31,32}. But the properties of rare-earth ions in smart-cut thin films have not yet been carefully explored.

Here we demonstrate an integrated photonic platform for rare-earth ions in a single crystal thin film which is compatible with scalable top down fabrication. The material stack is composed of smart-cut thin films of Tm^{3+} doped lithium niobate and wafer bonded onto silicon dioxide grown on a undoped lithium niobate substrate. Using this substrate, we pattern waveguides in the Tm^{3+} doped thin film and show strong optical absorption and spectral hole burning through waveguide transmission measurements. We compare the optical properties of the rare-earth ions in the waveguides to those in the bulk and find them to have virtually identical lifetimes and emission spectra, despite significant processing involved in smart-cut and patterning of the thin film. Furthermore, the smart-cut process induces negligible background emission in the substrate. Due to the small cross-sectional area of the waveguides patterned in a thin film, we are able to burn narrow spectral holes with powers that are over two orders of magnitude lower than in previously reported titanium in-diffused waveguides²⁸. These results demonstrate the suitability of these emitters for stable and spectrally narrow optical quantum memories, lasers, and filters in a thin film material that is compatible with wafer-scale processing and fabrication.

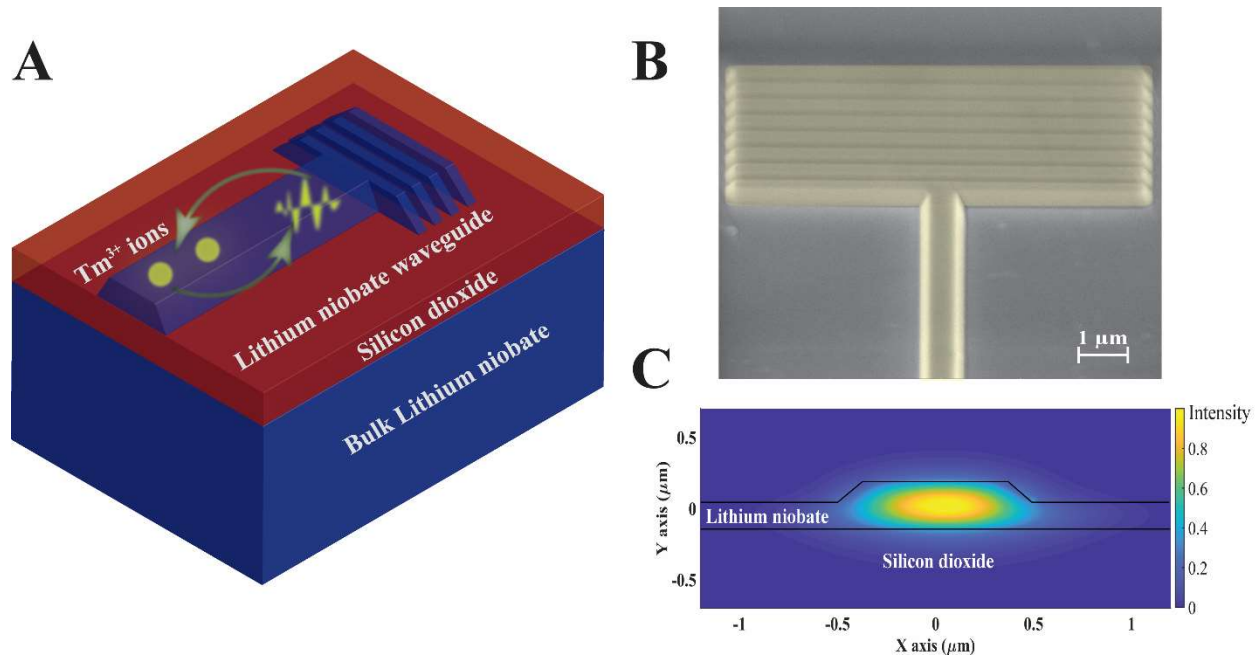


Figure 1. (A) Device geometry. Schematic of the cross-section of a waveguide etched in the heterogeneous material stack. (B) Scanning Electron Microscopy image of the waveguide with grating couplers patterned in the Tm^{3+} doped lithium niobate thin film. (C) Finite Difference Time Domain simulation showing the electric field distribution along the waveguide cross-section.

Fig 1(A) shows a schematic of the layer structure of the fabricated device. We begin with a bulk X-cut lithium niobate substrate doped with 0.1% Tm^{3+} . Using a commercial smart-cut process (NANOLN), we fabricate a 300 nm layer of doped single crystal lithium niobate wafer bonded to a 2 μm thick layer of silicon dioxide grown on undoped bulk lithium niobate as the substrate material. We etch waveguides into the doped thin film using a two-layer electron beam lithography and dry etching process (see Methods). Fig. 1(B) shows a scanning electron microscope image of the fabricated waveguide along with grating couplers to couple light from the out of plane dimension. The waveguides have smooth sidewalls etched at an angle of 45 degrees. We select the waveguide geometry to be single mode at 794 nm which is the ${}^3\text{H}_6 \rightarrow {}^3\text{H}_4$ optical transition for the Tm^{3+} ions. Fig. 1(C) shows a finite difference time domain simulation of the electric field intensity inside the waveguides for the fundamental TE mode at this wavelength. The waveguides are 700 nm wide and constitute only a partial etch of the thin film with an etch depth of 125 nm. Such a design minimizes the interaction of the light with the etched sidewalls resulting in low propagation losses³⁰. The optical mode exhibits transverse area of (176 nm X 400 nm) $0.07 \mu\text{m}^2$, which is over 2 orders of magnitude smaller than titanium in-diffused waveguides²⁸. The mode is tightly confined in the thin lithium niobate film where it interacts with the Tm^{3+} . The direction of the waveguide must be selected carefully so that the TE mode of the waveguide aligns with the dipole moment of the ions, which are oriented perpendicular to the optical axis (c axis) of the lithium niobate substrate^{19,28,33}. For comparison, we fabricated waveguides that are both parallel and orthogonal to the c axis.

To characterize the sample, we cool it down to 3.6 K in closed cycle cryostat (Attocube attoDRY). We use a confocal microscope with a diffraction limited spatial resolution between the excitation and the collection spots to perform photoluminescence and transmission measurements through the thin film waveguides. To perform broadband measurements, we excite the sample with a supercontinuum source (NKT Photonics) and detect the signal using a spectrometer (Princeton Instruments). For time-resolved measurements and spectral hole burning we use a single frequency laser (M Squared Solstis) modulated by gated acousto-optic modulators (Gooch and Housego) that carve out short pulses with a rise time of 350 ns, and also shift the frequency of the laser (see

Supporting Information Fig. S1). Pulses are detected using a single photon counting module (Excelitas Technologies Inc) with 400 ps temporal resolution.

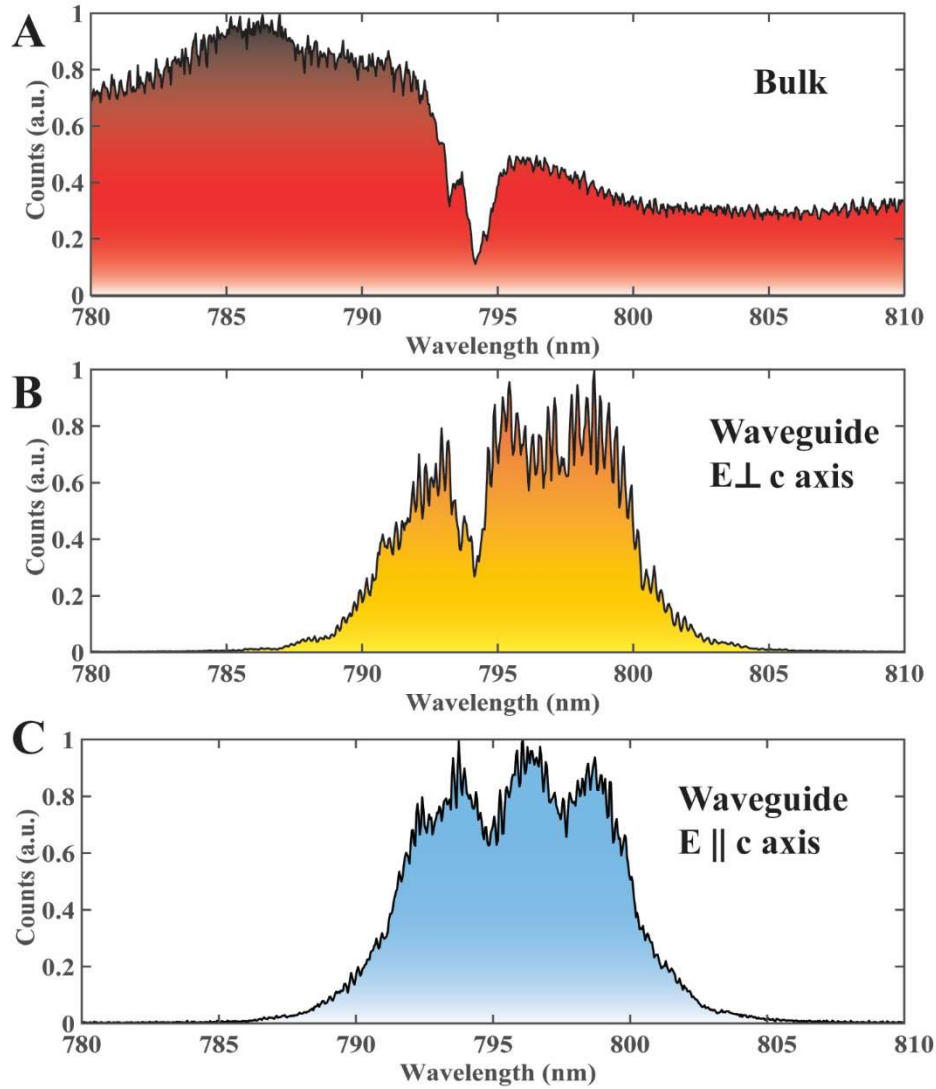


Figure 2. (A) Broadband transmission spectrum through a 1 mm length of Tm^{3+} doped bulk lithium niobate crystal with the electric field polarized perpendicular to the crystal c axis. (B)-(C) Broadband transmission spectrum filtered down to 10 nm, through a thin film waveguide with the electric field polarized perpendicular (B) and parallel (C) to the crystal c axis.

We first characterize the property of the bulk substrate (prior to smart-cut). To perform this measurement, we place the 500 μm -thick bulk substrate on top of a mirror and inject the beam

from the top. We excite the sample with the supercontinuum laser and collect the reflected light. In this way the beam performs a double-pass through the bulk and therefore goes through 1 mm of material. Fig. 2(A) shows the spectrum collected through the bulk crystal with the electric field polarization perpendicular to the crystal c axis. The bulk crystal exhibits a strong absorption peak at the wavelength range of 794 nm due to Tm^{3+} , which is consistent with past measurements³³. We observe a peak absorption of 75%, corresponding to an absorption coefficient of 14 cm^{-1} for the ions in the bulk crystal. This number is also consistent with past reported values for bulk Tm^{3+} in lithium niobate with similar doping densities³³. The sharp absorption peak disappears (not shown) when we orient the polarization parallel to the c axis, as expected due to the local crystal symmetry of the lattice sites occupied by Tm^{3+} ions in lithium niobate.³³.

Next, we probe the thin film by performing waveguide absorption measurements. We excite one end of the waveguide at the grating with a supercontinuum source, filtered to 10 nm using a bandpass interference filter, and collect from the grating coupler at the other end. Fig. 2(B) shows the transmission spectrum through a $775 \mu\text{m}$ long waveguide with the electric field polarized perpendicular to the crystal axis. The waveguide transmission exhibits the same sharp absorption peak as the bulk at 794 nm. We observe a peak absorption of 66% in the waveguide. This corresponds to an absorption coefficient of 14 cm^{-1} , consistent with the bulk value. Fig. 2(C) shows the transmission spectrum through an orthogonal waveguide with the electric field polarized parallel to the crystal c axis. We observe a small dip corresponding to a 30% absorption. This is attributed to the $240 \mu\text{m}$ bending regions in the long racetrack shaped waveguides where the polarization rotates along the bends and overlaps with the direction perpendicular to the crystal c axis. (see Supporting Information Fig. S2) These measurements indicate that the optical absorption of the ions in the thin film is highly polarized, and that the Tm^{3+} ions retain the bulk absorption properties even after significant nanofabrication steps. The fact that the absorption coefficient is nearly the same for both bulk and waveguides suggests that the waveguide transmission is dominated by the ion absorption, and not by fabrication imperfections in the waveguide that can cause additional undesired loss.

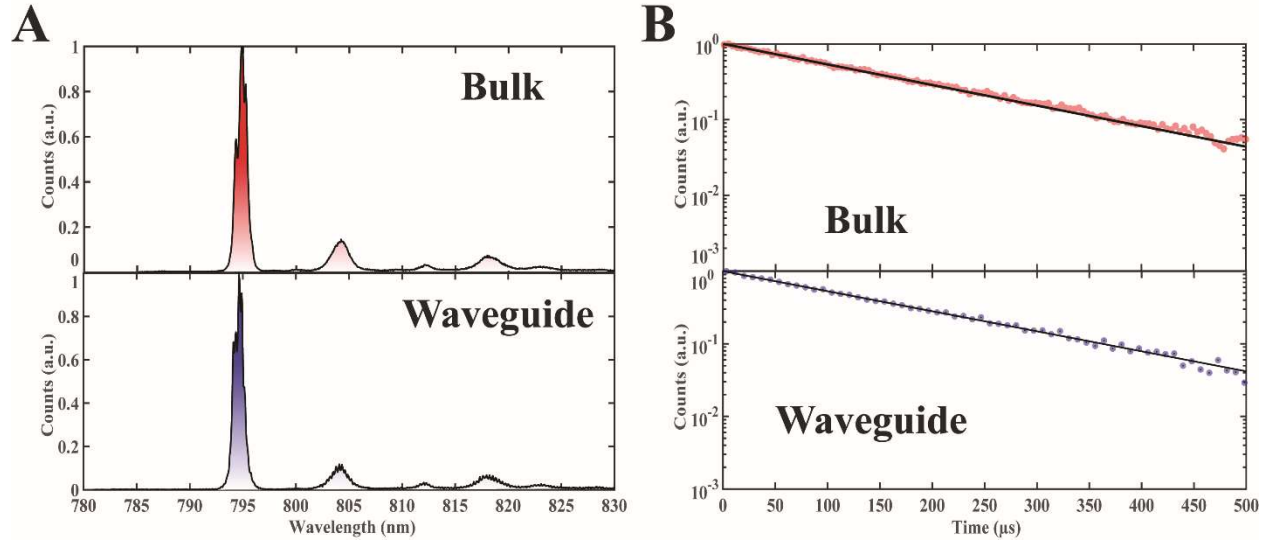


Figure 3. (A) Photoluminescence spectrum from bulk crystal and a waveguide in Tm^{3+} doped lithium niobate thin film. (B) Time resolved photoluminescence through a thin film waveguide and bulk crystal respectively. The solid black lines denote a fit to a single exponential decay. The fit reveals lifetimes of $157.4 \pm 1.5 \mu\text{s}$ and $158 \pm 2.8 \mu\text{s}$ in the thin film and bulk respectively.

The inhomogeneous linewidth of the rare-earth ion ensemble is a good measure of the residual lattice strain in the host material. The spectral line shape reflects the local crystal field experienced by the ions. To further probe these properties, we perform photoluminescence spectroscopy of the ions in the bulk sample and the thin film waveguide. We use a narrow tunable laser (M Squared Solstis) to excite the fifth level of the $^3\text{H}_4$ excited state multiplet at 773.3925 nm. At 3.6 K the population relaxes to the lowest level of the excited state multiplet by phonon emission on a timescale much shorter than the fluorescence lifetime³³. Fig 3(A) shows the photoluminescence spectra through the bulk sample and the thin film waveguides. Both spectra reveal similar line shapes for all the transitions from the lowest level of the excited state to the ground state multiplet. The bulk luminescence has a full width at half maximum of $0.7 \pm 0.01 \text{ nm}$ which is similar to the $0.69 \pm 0.01 \text{ nm}$ measured for the thin film waveguide. Furthermore, we do not observe appreciable background fluorescence³⁴ induced by the smart-cut process, which indicates that this process does not generate substantial fluorescence centers that can pollute the Tm^{3+} fluorescence.

In order to ascertain whether the smart-cut process introduces unwanted non-radiative decay, we perform time-resolved photoluminescence measurements. Additional non-radiative decay of

in the thin film would lead to a shortened optical lifetime^{28,35–37} or non-exponential luminescence decay³⁶. We perform time-resolved photoluminescence on the ions in the thin film waveguides and the bulk using a modulated single frequency laser with a center frequency at 773.3925 nm. A gated acousto-optic modulator carves out the excitation laser into short pulses (see Supporting Information Fig. S1). Fig 3(B) shows the time resolved photoluminescence signal from a 15 μm long thin film waveguide and the bulk sample. Both the spectra are fit to a single exponential decay and reveal spontaneous emission lifetimes of $157.4 \pm 1.5 \mu\text{s}$ and $158 \pm 2.8 \mu\text{s}$ respectively, which are equivalent to within the sensitivity of the measurement. We therefore do not observe any additional source of non-radiative decay in the thin film material.

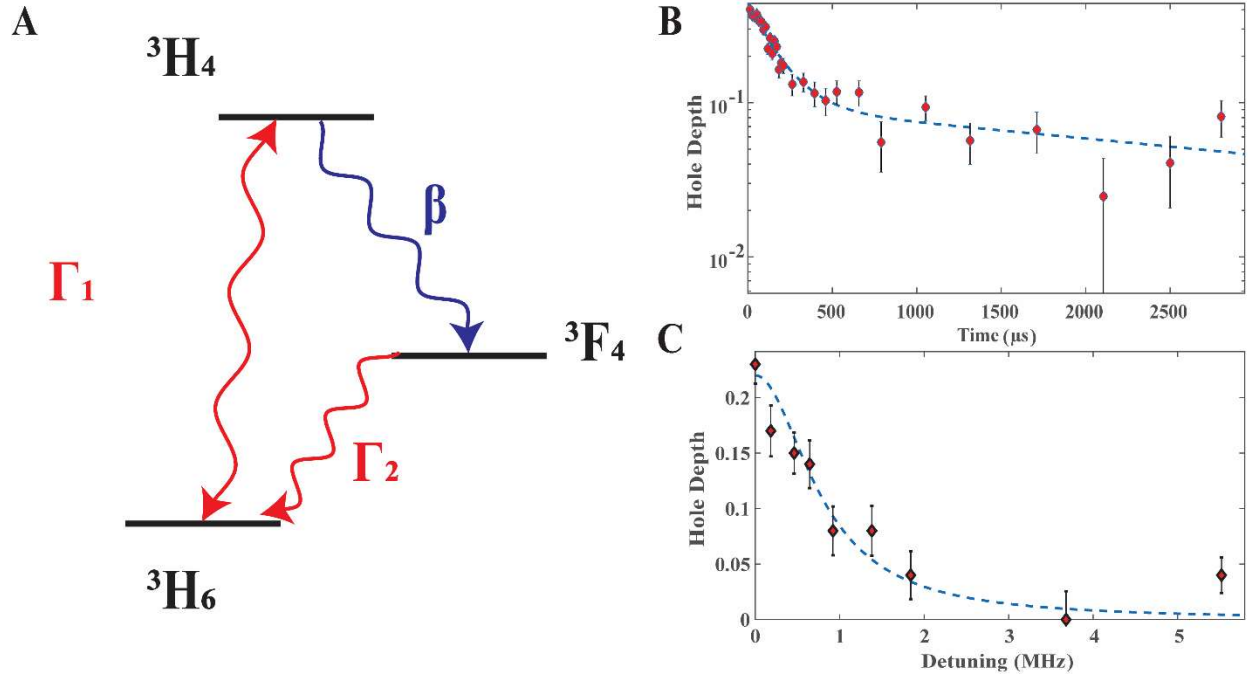


Figure 4. (A) Simplified energy level structure of Tm^{3+} ions in a lithium niobate thin film. Γ_1 and Γ_2 denote the decay rates from ${}^3\text{H}_4$ and ${}^3\text{F}_4$ to ${}^3\text{H}_6$ respectively. β denotes the branching ratio of the transition from ${}^3\text{H}_4$ to ${}^3\text{F}_4$. (B) Time resolved decay of a spectral hole in a thin film waveguide. The dashed line shows a fit to a biexponential decay. (C) Frequency resolved decay of a spectral hole in a thin film waveguide. The dashed line shows a fit to a Lorentzian profile.

One of the key features of a rare-earth ion ensemble is the ability to tailor the inhomogeneously broadened absorption profile by burning spectral holes. Spectral hole burning is a critical step for many applications in both classical and quantum optics⁴. A narrow spectral hole acts as a high quality factor frequency filter for optical signal processing^{4,8}, and also enables atomic frequency combs that are an essential step for ensemble optical quantum memory protocols^{19,38}. Tm^{3+} ions in crystalline lithium niobate have a level structure as shown in Fig. 4(A) which allows for spectral hole burning^{19,28,33,39}. Atoms excited to the $^3\text{H}_4$ state either decay back to the ground state $^3\text{H}_6$ level or to a metastable state $^3\text{F}_4$ via two dominant pathways. The shelving state has a long lifetime of several milliseconds. It acts as a population trap before finally decaying back to the ground state. This population trapping allows us to burn a spectral hole in Tm^{3+} .

To burn a spectral hole, we split the single frequency laser into two acousto-optic modulators to separately generate a burn pulse and a probe pulse (see Supporting Information Fig. S1). Varying time delays between the burn and the probe pulses maps out the decay of the spectral hole. Fig 4(B) plots the decay of a spectral hole burned at 794 nm in a waveguide patterned on the Tm^{3+} doped thin film. The plot follows a bi-exponential decay with lifetimes of $162 \pm 16 \mu\text{s}$ (Γ_1) and $3 \pm 1.6 \text{ ms}$ (Γ_2) and a branching ratio (β) of $22 \pm 6 \%$. These lifetimes correspond to the spontaneous emission rate of the $^3\text{H}_4$ and the decay of the metastable $^3\text{F}_4$ respectively, while the branching ratio corresponds to the decay of the $^3\text{H}_4$ excited state to the metastable state. The values are consistent with previous measurements performed in bulk crystals³³. These results suggest that ion sliced materials can be used for atomic frequency combs with similar performance to bulk structures, but in a compact integrated photonic form-factor.

The linewidth of the spectral holes puts a limit on the storage time of the optical quantum memories^{19,34,36}. To measure this linewidth, we attenuate the laser burn power and burn a spectral hole to partial depth to limit power broadening. We scan the probe frequency with respect to the burn pulse and map out the decay of the spectral hole. Fig. 4(C) shows the decay of the spectral hole when fit to a Lorentzian profile. The fit shows a linewidth of $1.6 \pm 0.4 \text{ MHz}$. The inverse of the spectral hole linewidth puts a lower bound on the optical coherence time at $0.66 \pm 0.16 \mu\text{s}$. This value is already close to previous reports of a $1.6 \mu\text{s}$ coherence time of at 3.6 K,^{28,33,39}

measured using spin-echo. The difference between these measurements is likely due to power broadening and instantaneous spectral diffusion caused by the process of burning a hole and also by instabilities in the laser linewidth in the course of the measurement. Further experiments using two photon echo schemes would provide a more accurate measurement of the actual coherence time of the system.

One advantage of the thin film platform is that it enables waveguides with significantly smaller cross-sectional areas, which significantly reduces the power required to burn spectral holes. Our waveguides have a mode cross sectional area of only $0.07 \mu\text{m}^2$ which is 500 times smaller than that of titanium in-diffused waveguides²⁸ in bulk lithium niobate. Thus, we expect to be able to burn spectral holes with much less power than that in bulk waveguides. To estimate the power in the waveguide mode we measure the end to end efficiency of the setup from the objective lens that focuses the light onto the input grating coupler, to the collection fiber that collects light from the output grating coupler. We measure this efficiency to be 10^{-6} . We assume that the efficiencies of the input and output grating coupler are the same, resulting in a coupling efficiency of about 10^{-3} for each coupler. Using this efficiency, we calculate that the peak power required to burn a hole to transparency in the waveguide using a $12.5 \mu\text{s}$ long laser pulse is only 10 nW. This is over two orders of magnitudes lower than previously reported values in bulk waveguides for the same length of the burn pulse²⁸.

In conclusion, we demonstrate an integrated photonic platform for rare-earth ions in a single crystal thin film which is compatible with scalable planar fabrication. Our technique preserves the desirable optical properties of the rare-earth ions in bulk crystal, paving the way for on-chip lasing, optical signal processing and quantum memory. Lithium niobate also has a strong piezo-electric coefficient that can tune and modulate the ion resonant frequencies to achieve controlled reversible inhomogeneous broadening of narrow absorption lines^{28,38}. Reducing the waveguide dimensions by going to a thin film substrate enables the creation of strong electric fields at lower voltages and higher bandwidths⁴⁰, which would significantly enhance the speed at which the ions can be tuned. Other rare-earth ion species such as Er^{3+} and Pr^{3+} can also be doped into the substrate to enable other wavelength ranges including the telecom band^{20,29}. Patterning the substrate into nanophotonic cavities³¹ could further enhance light-matter interactions, providing a pathway for

spin-photon interfaces^{41–43}. Ultimately, our results add tremendous functionality to the emerging field of lithium niobate integrated photonics by providing a compact and versatile optically active material that has broad applications in both classical and quantum optics.

Methods

Device Fabrication: To pattern the thin film waveguide we first grow a 500 nm layer of amorphous silicon which acts as a hard mask. We spin a 300 nm layer of ZEP520A and pattern the samples using a 100 kV electron beam lithography system (Elionix). We deposit 10 nm chromium in an electron beam evaporator and perform metal liftoff to make a negative mask. Using chromium as a mask we first etch the silicon with a standard fluorine chemistry dry etching recipe. Now, with the silicon as a hard mask we transfer the pattern to the thin film lithium niobate using an optimized argon plasma physical etching technique. Finally, we use a 30% solution of KOH at 80° C to remove the remaining silicon. We grow a 2 μm layer of oxide on top of the waveguides to reduce scattering induced losses at the waveguide sidewalls.

AUTHOR INFORMATION

Corresponding Author

edowaks@umd.edu

Author Contributions

S. D. and E. W. conceived the experiments. S. D., E. A. G. and E. W. designed the experiments and prepared the manuscript. S. D. conducted the measurements and analyzed the data. S. B. contributed to the optical setup and measurements. U. S. contributed to sample fabrication.

Funding Sources

This work was supported by the National Science Foundation (grant number EFMA1741651), the Air Force Office of Scientific Research MURI FA95501910172, the ARL Center for Distributed Quantum Information, and the Physics Frontier Center at the Joint Quantum Institute.

Acknowledgements

The authors declare no competing financial interests.

Supporting Information Available

We provide supporting information for the waveguide absorption measurements and the optical setup for time resolved photoluminescence and spectral hole burning measurements.

- (1) Thiel, C. W.; Sun, Y.; Macfarlane, R. M.; Böttger, T.; Cone, R. L. Rare-Earth-Doped LiNbO₃ and KTiOPO₄ (KTP) for Waveguide Quantum Memories. *J. Phys. B At. Mol. Opt. Phys.* **2012**, *45* (12). <https://doi.org/10.1088/0953-4075/45/12/124013>.
- (2) Kunkel, N.; Goldner, P. Recent Advances in Rare Earth Doped Inorganic Crystalline Materials for Quantum Information Processing. *Zeitschrift für Anorg. und Allg. Chemie* **2018**, *644* (2), 66–76. <https://doi.org/10.1002/zaac.201700425>.
- (3) Zhong, T.; Goldner, P. Review Article Emerging Rare-Earth Doped Material Platforms for Quantum Nanophotonics. **2019**, *8* (11), 2003-2015. <https://doi.org/10.1515/nanoph-2019-0185>.
- (4) Thiel, C. W.; Böttger, T. Rare-Earth-Doped Materials with Application to Optical Signal Processing , Quantum Information Science , and Medical Imaging Technology. **2012**, Proc. SPIE 8272, 82720E. <https://doi.org/10.1117/12.909154>.
- (5) Kane, T. J.; Byer, R. L. Monolithic, Unidirectional Single-Mode Nd:YAG Ring Laser. *Opt. Lett.* **1985**, *10* (2), 65–67. <https://doi.org/10.1364/OL.10.000065>.
- (6) Equall, R. W.; Sun, Y.; Cone, R. L.; Macfarlane, R. M. Ultraslow Optical Dephasing in Eu³⁺:Y₂SiO₅. *Phys. Rev. Lett.* **1994**, *72* (14), 2179–2182. <https://doi.org/10.1103/PhysRevLett.72.2179>.
- (7) Böttger, T.; Thiel, C. W.; Cone, R. L.; Sun, Y. Effects of Magnetic Field Orientation on Optical Decoherence in Er³⁺:Y₂SiO₅. *Phys. Rev. B* **2009**, *79* (11), 115104. <https://doi.org/10.1103/PhysRevB.79.115104>.
- (8) Thiel, C. W.; Böttger, T.; Cone, R. L. Rare-Earth-Doped Materials for Applications in Quantum Information Storage and Signal Processing. *J. Lumin.* **2011**, *131* (3), 353–361. <https://doi.org/https://doi.org/10.1016/j.jlumin.2010.12.015>.

- (9) Li, Y.; Zhang, H.; Kim, C.; Wagner, K. H.; Hemmer, P.; Wang, L. V. Pulsed Ultrasound-Modulated Optical Tomography Using Spectral-Hole Burning as a Narrowband Spectral Filter. *Appl. Phys. Lett.* **2008**, *93* (1), 11111. <https://doi.org/10.1063/1.2952489>.
- (10) Zhong, M.; Hedges, M. P.; Ahlefeldt, R. L.; Bartholomew, J. G.; Beavan, S. E.; Wittig, S. M.; Longdell, J. J.; Sellars, M. J. Optically Addressable Nuclear Spins in a Solid with a Six-Hour Coherence Time. *Nature* **2015**, *517*, 177-180. <https://doi.org/10.1038/nature14025>.
- (11) Heinze, G.; Hubrich, C.; Halfmann, T. Stopped Light and Image Storage by Electromagnetically Induced Transparency up to the Regime of One Minute. **2013**, *033601*, 1–5. <https://doi.org/10.1103/PhysRevLett.111.033601>.
- (12) Wesenberg, J. H.; Molmer, K.; Rippe, L.; Kröll, S. Scalable Designs for Quantum Computing with Rare-Earth-Ion-Doped Crystals. *Phys. Rev. A* **2007**, *75* (1), 12304. <https://doi.org/10.1103/PhysRevA.75.012304>.
- (13) Kimble, H. J. The Quantum Internet. *Nature* **2008**, *453* (7198), 1023–1030. <https://doi.org/10.1038/nature07127>.
- (14) Sangouard, N.; Simon, C.; de Riedmatten, H.; Gisin, N. Quantum Repeaters Based on Atomic Ensembles and Linear Optics. *Rev. Mod. Phys.* **2011**, *83* (1), 33–80. <https://doi.org/10.1103/RevModPhys.83.33>.
- (15) Chen, Y. Nanofabrication by Electron Beam Lithography and Its Applications: A Review. *Microelectron. Eng.* **2015**, *135*, 57–72. <https://doi.org/https://doi.org/10.1016/j.mee.2015.02.042>.
- (16) Zhong, T.; Kindem, J. M.; Rochman, J.; Faraon, A. Interfacing Broadband Photonic Qubits to On-Chip Cavity-Protected Rare-Earth Ensembles. **2017**, *8* (14107), 1–7. <https://doi.org/10.1038/ncomms14107>.
- (17) Zhong, T.; Kindem, J. M.; Bartholomew, J. G.; Rochman, J.; Craiciu, I.; Verma, V.; Nam, S. W.; Marsili, F.; Shaw, M. D.; Beyer, A. D.; et al. Optically Addressing Single Rare-Earth Ions in a Nanophotonic Cavity. *Phys. Rev. Lett.* **2018**, *121* (18), 183603. <https://link.aps.org/doi/10.1103/PhysRevLett.121.183603>.

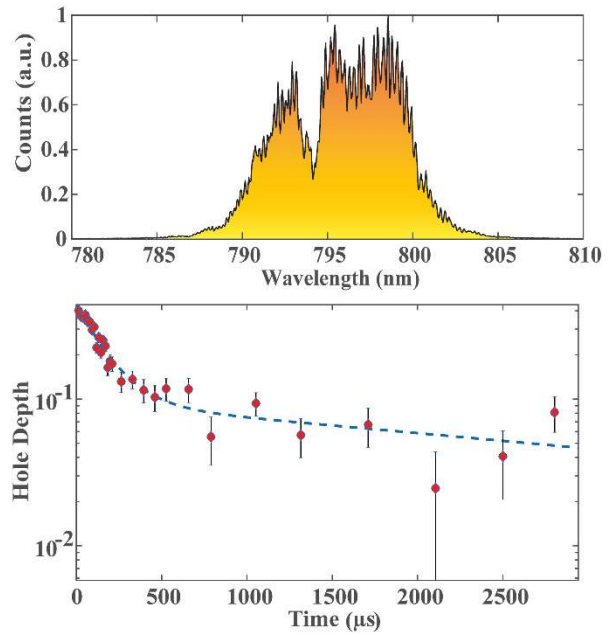
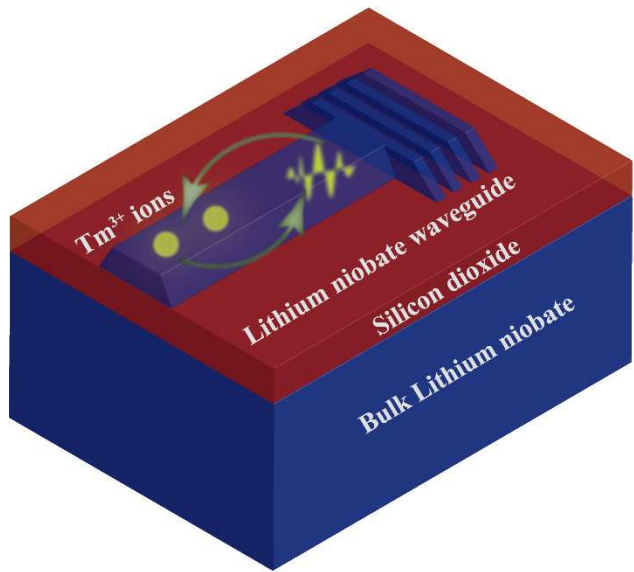
- (18) Zhong, T.; Kindem, J. M.; Bartholomew, J. G.; Rochman, J.; Craiciu, I.; Miyazono, E.; Bettinelli, M.; Cavalli, E.; Verma, V.; Nam, S. W.; et al. Nanophotonic Rare-Earth Quantum Memory with Optically Controlled Retrieval. *Science*. **2017**, *357* (6358), 1392-1395. <https://doi.org/10.1126/science.aan5959>.
- (19) Saglamyurek, E.; Sinclair, N.; Jin, J.; Slater, J. A.; Oblak, D.; Bussi eres, F.; George, M.; Ricken, R.; Sohler, W.; Tittel, W. Broadband Waveguide Quantum Memory for Entangled Photons. *Nature*. **2011**, *469*, 512–515. <https://doi.org/10.1038/nature09719>.
- (20) Dibos, A. M.; Raha, M.; Phenicie, C. M.; Thompson, J. D. Atomic Source of Single Photons in the Telecom Band. **2018**, *243601*, 1–6. <https://doi.org/10.1103/PhysRevLett.120.243601>.
- (21) Jiang, X.; Pak, D.; Nandi, A.; Xuan, Y.; Hosseini, M. Rare Earth-Implanted Lithium Niobate: Properties and on-Chip Integration. *Appl. Phys. Lett.* **2019**, *115* (7), 71104. <https://doi.org/10.1063/1.5098316>.
- (22) Miyazono, E.; Craiciu, I.; Arbabi, A.; Zhong, T.; Faraon, A. Coupling Erbium Dopants in Yttrium Orthosilicate to Silicon Photonic Resonators and Waveguides. *Optics Express* **2017**, *7* (3), 2863–2871. <https://doi.org/10.1364/OE.25.002863>.
- (23) Ding, D.; Pereira, L. M. C.; Bauters, J. F.; Heck, M. J. R.; Welker, G.; Vantomme, A.; Bowers, J. E.; Dood, M. J. A. De; Bouwmeester, D. Multidimensional Purcell Effect in an Ytterbium-Doped Ring Resonator. *Nat. Photonics* **2016**, *10*, 385-388. <https://doi.org/10.1038/NPHOTON.2016.72>.
- (24) Gong, Y.; Makarova, M.; Yerci, S.; Li, R.; Stevens, M. J.; Baek, B.; Nam, S. W.; Hadfield, R. H.; Dorenbos, S. N.; Zwiller, V.; et al. Linewidth Narrowing and Purcell Enhancement in Photonic Crystal Cavities on an Er-Doped Silicon Nitride Platform. *Opt. Express* **2010**, *18* (3), 2601–2612. <https://doi.org/10.1364/OE.18.002601>.
- (25) Gong, Y.; Makarova, M.; Yerci, S.; Li, R.; Stevens, M. J.; Baek, B.; Nam, S. W.; Dal Negro, L.; Vučković, J. Observation of Transparency of Erbium-Doped Silicon Nitride in Photonic Crystal Nanobeam Cavities. *Opt. Express* **2010**, *18* (13), 13863–13873. <https://doi.org/10.1364/OE.18.013863>.

- (26) Becker, P.; Brinkmann, R.; Dinand, M.; Sohler, W.; Suche, H. Er-diffused Ti:LiNbO₃ Waveguide Laser of 1563 and 1576 Nm Emission Wavelengths. *Appl. Phys. Lett.* **1992**, *61* (11), 1257–1259. <https://doi.org/10.1063/1.107610>.
- (27) Brüske, D.; Sunstov, S.; Rüter, C. E.; Kip, D. Efficient Nd:Ti:LiNbO₃ Ridge Waveguide Lasers Emitting around 1085 Nm. *Opt. Express* **2019**, *27* (6), 8884–8889. <https://doi.org/10.1364/OE.27.008884>.
- (28) Sinclair, N.; Saglamyurek, E.; George, M.; Ricken, R.; La Mela, C.; Sohler, W.; Tittel, W. Spectroscopic Investigations of a Ti: Tm LiNbO₃ Waveguide for Photon-Echo Quantum Memory. *Journal of Luminescence*, **2010**, *130* (9), 1586-1593. <https://doi.org/10.1016/j.jlumin.2009.12.022>.
- (29) Staudt, M. U.; Afzelius, M.; de Riedmatten, H.; Hastings-Simon, S. R.; Simon, C.; Ricken, R.; Suche, H.; Sohler, W.; Gisin, N. Interference of Multimode Photon Echoes Generated in Spatially Separated Solid-State Atomic Ensembles. *Phys. Rev. Lett.* **2007**, *99* (17), 173602. <https://doi.org/10.1103/PhysRevLett.99.173602>.
- (30) Zhang, M.; Wang, C.; Cheng, R.; Shams-Ansari, A.; Loncar, M. Monolithic Ultrahigh-Q Lithium Niobate Microring Resonator. *Optica* **2017**, *4* (12), 1536-1537. <https://doi.org/10.1364/OPTICA.4.001536>.
- (31) Li, M.; Liang, H.; Luo, R.; He, Y.; Lin, Q. High-Q 2D Lithium Niobate Photonic Crystal Slab Nanoresonators. *Laser & Photonics Reviews* **2019**, *13* (1800228), 1–8. <https://doi.org/10.1002/lpor.201800228>.
- (32) Liang, H.; Luo, R.; He, Y.; Jiang, H.; Lin, Q. High-Quality Lithium Niobate Photonic Crystal Nanocavities. *Optica* **2017**, *4* (10), 1251-1258. <https://doi.org/10.1364/OPTICA.4.001251>.
- (33) Sun, Y.; Thiel, C. W.; Cone, R. L. Optical Decoherence and Energy Level Structure of 0.1% Tm³⁺:LiNbO₃. *Phys. Rev. B* **2012**, *85*, 165106. <https://doi.org/10.1103/PhysRevB.85.165106>.
- (34) Magyar, A.; Hu, W.; Shanley, T.; Flatté, M. E.; Hu, E.; Aharonovich, I. Synthesis of Luminescent Europium Defects in Diamond. *Nat. Commun.* **2014**, *5* (1), 3523.

<https://doi.org/10.1038/ncomms4523>.

- (35) Sinclair, N.; Oblak, D.; Thiel, C. W.; Cone, R. L.; Tittel, W. Properties of a Rare-Earth-Ion-Doped Waveguide at Sub-Kelvin Temperatures for Quantum Signal Processing. *Phys. Rev. Lett.* **2017**, *118* (10), 100504 <https://doi.org/10.1103/PhysRevLett.118.100504>.
- (36) Scarafagio, M.; Tallaire, A.; Tielrooij, K.-J.; Cano, D.; Grishin, A.; Chavanne, M.-H.; H. L. Koppens, F.; Ringuedé, A.; Cassir, M.; Serrano, D.; et al. Ultrathin Eu- and Er-Doped Y2O3 Films with Optimized Optical Properties for Quantum Technologies. *J. Phys. Chem. C* **2019**, *123* (21), 13354–13364. <https://doi.org/10.1021/acs.jpcc.9b02597>.
- (37) Flinn, G. P.; Jang, K. W.; Ganem, J.; Jones, M. L.; Meltzer, R. S.; Macfarlane, R. M. Anomalous Optical Dephasing in Crystalline Y₂O₃: Eu³⁺. *J. Lumin.* **1994**, *58* (1), 374–379. [https://doi.org/https://doi.org/10.1016/0022-2313\(94\)90441-3](https://doi.org/https://doi.org/10.1016/0022-2313(94)90441-3).
- (38) Chanelière, T.; Hétet, G.; Sangouard, N.. Quantum Optical Memory Protocols in Atomic Ensembles. *Advances In Atomic, Molecular, and Optical Physics* **2018**, *67*, 77–150. <https://doi.org/10.1016/bs.aamop.2018.02.002>.
- (39) Thiel, C. W.; Sun, Y.; Bttger, T.; Babbitt, W. R.; Cone, R. L. Optical Decoherence and Persistent Spectral Hole Burning in Tm³⁺:LiNbO₃. *Journal of Luminescence* **2010**, *130* (9), 1598-1602. <https://doi.org/10.1016/j.jlumin.2009.12.019>.
- (40) Wang, C. H.; Zhang, M.; Stern, B.; Lipson, M.; Lončar M.. Nanophotonic Lithium Niobate Electro-Optic Modulators. **2018**, *26* (2), 1547–1555. <https://doi.org/10.1364/OE.26.001547>.
- (41) Nguyen, C. T.; Sukachev, D. D.; Bhaskar, M. K.; Machielse, B.; Levonian, D. S.; Knall, E. N.; Stroganov, P.; Riedinger, R.; Park, H.; Lončar, M.; et al. Quantum Network Nodes Based on Diamond Qubits with an Efficient Nanophotonic Interface. *Phys. Rev. Lett.* **2019**, *123* (18), 183602. <https://doi.org/10.1103/PhysRevLett.123.183602>.
- (42) Sun, S.; Kim, H.; Luo, Z.; Solomon, G. S.; Waks, E. A Single-Photon Switch and Transistor Enabled by a Solid-State Quantum Memory. *Science* **2018**, *361* (6397), 57 – 60. <https://doi.org/10.1126/science.aat3581>.
- (43) Wilk, T.; Webster, S. C.; Kuhn, A.; Rempe, G. Single-Atom Single-Photon Quantum

Table of Content Graphic



Supporting Information

An Integrated Photonic Platform for Rare-Earth Ions in Thin Film Lithium Niobate

Subhojit Dutta¹, Elizabeth A. Goldschmidt², Sabyasachi Barik¹, Uday Saha¹, Edo Waks^{1*}

¹Department of Electrical and Computer Engineering, Institute for Research in Electronics and Applied Physics, and Joint Quantum Institute, University of Maryland, College Park, MD 20742, USA.

*²Department of Physics, University of Illinois at Urbana-Champaign, Urbana, IL 61801
edowaks@umd.edu

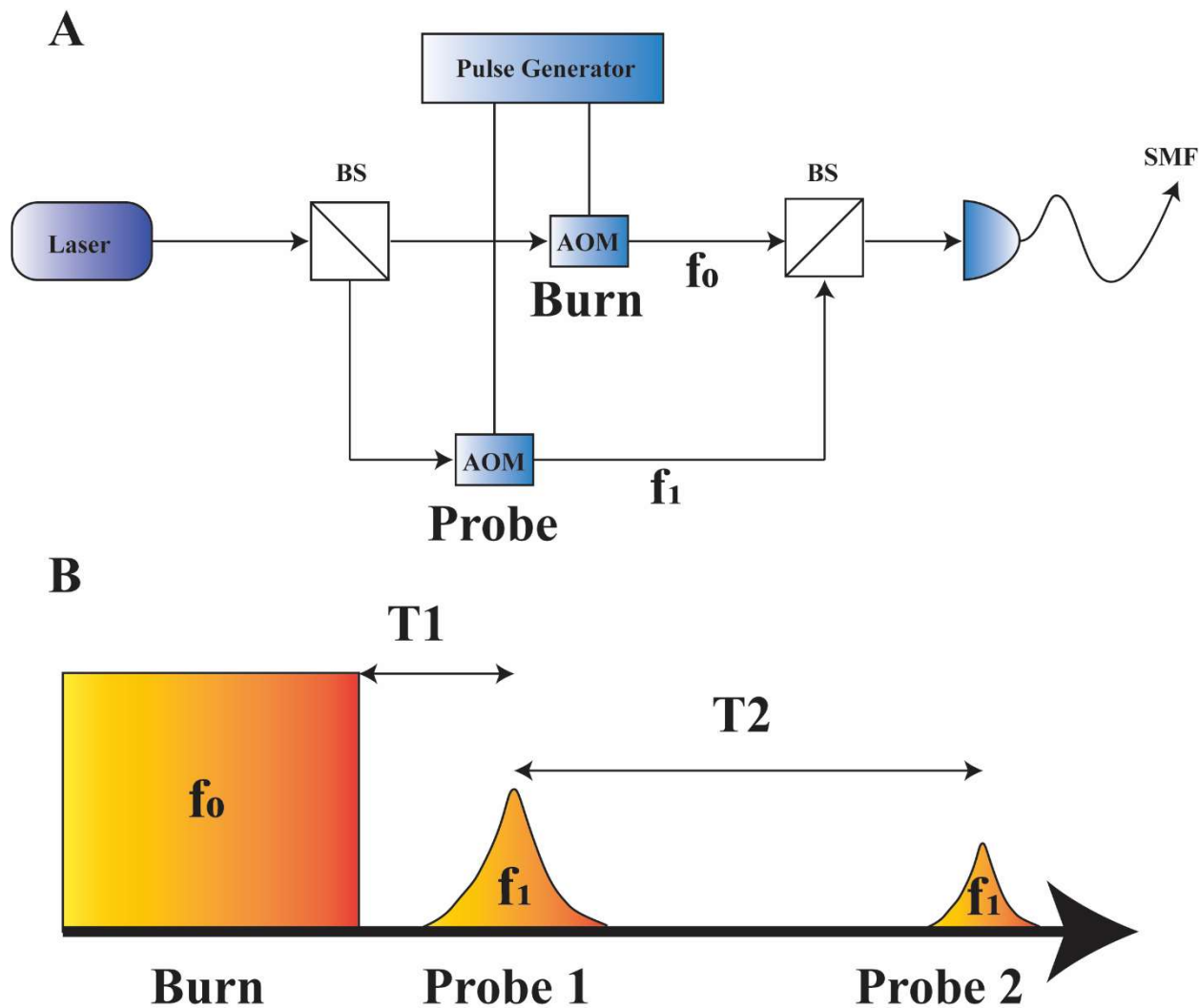


Figure S1. (A) Schematic of the setup for generating optical pulses. Laser, Single Frequency MSquared Solistis; BS, Beam Splitter; AOM, Acousto-optic modulator; SMF, Single Mode Fiber; f_0 , Burn frequency; f_1 , Probe frequency. (B) Pulse sequence for time and frequency resolved spectral hole burning. T1 denotes the delay between the Burn and Probe1. T2 denotes the delay between Probe1 and Probe2.

Time Resolved Photoluminescence Experiments: For time resolved photoluminescence we carve out 500 ms long pulses using one of the AOMs, at 773.3925 nm to excite the fifth level of the 3H_4 excited state multiplet in the Tm^{3+} ions. We record the time resolved decay of the photoluminescence signal on a single photon counting module (Excelitas Technologies Inc), spectrally filtered down to a width of 0.1 nm using a spectrometer (Princeton instruments) as a filter.

Spectral Hole Burning Experiments: To perform spectral hole burning measurements we use two AOMs to carve out pulses at two independent frequencies, f_0 and f_1 , from the single frequency

input laser. We can switch the AOMs by means of an RF switch (Mini circuits) and control pulses generated by an arbitrary function generator (Tektronix). We drive the AOMs using a pair of Voltage Controlled Oscillators (Mini circuits) which can be tuned to independently control the output frequencies f_0 and f_1 .

- 1) For time resolved spectral hole burning experiments, we use a $12.5 \mu\text{s}$ long burn pulse with a pulse power of $30 \mu\text{W}$ before the objective lens, at a frequency f_0 . We generate a probe with a pulse power of about $0.3 \mu\text{W}$ before the objective lens. We tune the frequencies of the burn and the probe pulses on resonances by interfering them on a fast photodetector (Thorlabs) and minimizing the observed beat frequency. To perform the experiment, we use a long delay, T_2 of about 5 ms between two probe pulses vary the delay T_1 . The difference in the integrated area between the two probes represents the depth of a spectral hole at a time, T_1 .
- 2) For frequency resolved spectral hole burning experiments, we attenuate the burn pulse to about $3 \mu\text{W}$ before the objective lens. Keeping T_1 and T_2 fixed we sweep the frequency, f_1 of the of the probe with respect to the frequency f_0 of the burn pulse and map out the difference in the integrated areas between the two probe pulses which represents the hole depth.

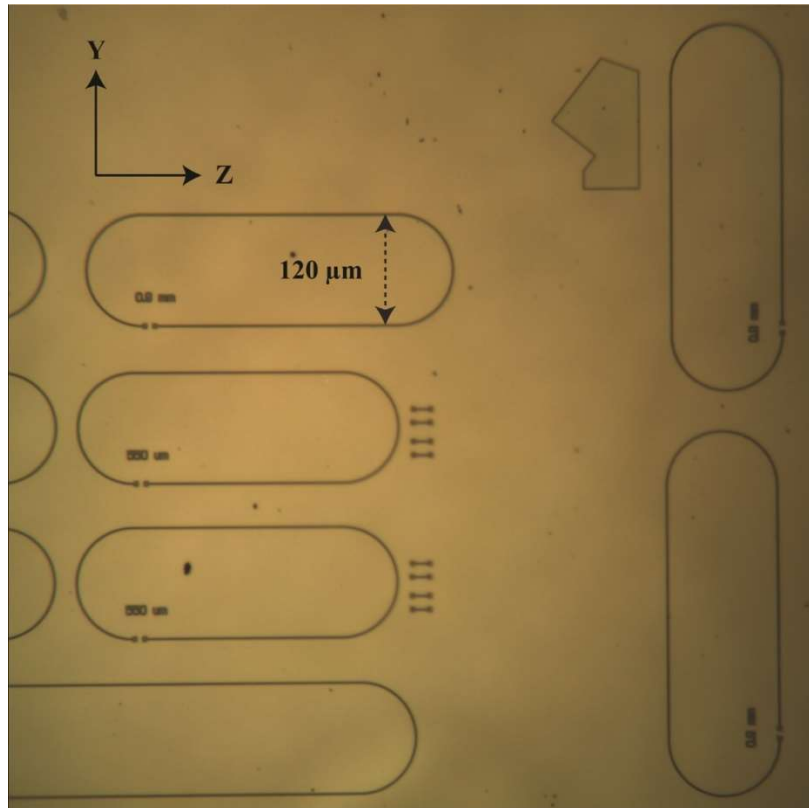


Figure S2. Optical microscope image of a representative sample. The crystal c axis is oriented along the Z direction. Racetrack shaped waveguides are fabricated orthogonally with respect to the c axis of the crystal.

Waveguide Absorption Experiments: Figure S2 shows a widefield optical microscope image of racetrack shaped waveguides fabricated in thin film lithium niobate oriented orthogonal and parallel to the crystal axis. Our measurement microscope has a 40 μm wide field of view. To accommodate both the excitation and the collection within the same field of view we fabricate long racetrack shaped waveguides that wrap around. As a result, the polarization of light rotates along the bends and overlaps with the orthogonal direction.